appliedoptics

Surface figure compensation of the primary mirror in a Ritchey–Chrétien space telescope by spring preloads

Shuqiang Jia,[1,2] **Wei Huang,**[1,*] **Mingfei Xu,**[1] **and Xin Qin**[1,2]

[1] *State Key Laboratory of Applied Optics, Changchun Institute of Optics, Fine Mechanics and Physics, Chinese Academy of Sciences, Changchun 130033, China*
[2] *University of Chinese Academy of Science, Beijing 100049, China*
*Corresponding author: huangw@ciomp.ac.cn

To reduce the surface figure error induced by mechanical strains during the integration process of a high-precision mirror, a cost-efficient compensation method by spring preloads is proposed. The study is based on the primary mirror of a Ritchey–Chrétien space telescope with a focal length of 1200 mm. First, the surface figure degradation of the mirror during the assembly process is expressed and analyzed. Then, a finite element model of the mirror and its mounting structure is established, and surface deformations caused by different preloading forces are simulated. An optimized combination of different preloads was obtained through data fitting, and the influence of the combined preload on the mirror was analyzed. The simulation results show that ring preloads mainly affect spherical aberration and high-order spherical aberrations, while quadrupole preloads mainly affect astigmatism, and the optimized preload can compensate for the surface figure error from 0.120λ RMS to 0.088λ RMS. Last, the surface figure error of the mirror is measured by experiments under optimized preloads, and the result is 0.084λ RMS, which verifies the correctness of the analysis process and effectiveness of the compensation method.   © 2023 Optica Publishing Group

1. INTRODUCTION

Cassegrain-type space telescope is a common optical facility on artificial satellites [1–5]. With the development of remote sensing technology in the field of small satellites and commercial satellites [4–8], more and more satellite systems need space optical payloads with small package sizes, light weight, and low manufacturing cost while ensuring a certain resolution of Earth observation. Generally, the primary mirror with the largest aperture in a Cassegrain optical system is one of the most expensive components and is difficult to process. The surface figure accuracy of the primary mirror has important impacts on wavefront aberrations of an optical system, and reducing the surface figure errors of the primary mirror is an efficient way to improve the performance of the optical system.

Surface figure errors of a mirror mainly come from machining errors [9–11], deformations caused by the bonding process [12–14], stresses and strains in the assembly process [15,16], and thermal deformations caused by temperature changes [17,18], which affect wavefront aberrations of optical systems significantly. There are usually two ways to reduce wavefront aberrations of optical systems, which are active optics and compliant compensation. One way to realize active optics is to add a relay mirror to the optical system; the surface figure of the relay

mirror can be controlled actively. For example, a single point actuator is used to control the spherical aberration or cylindric error of relay mirrors to compensate for wavefront aberrations of optical systems [18–20]. Another way to realize active optics is to set actuators directly on optical elements. Optical surfaces are deformed deliberately to compensate for wavefront aberrations of optical systems by controlling forces or displacements of the actuators [21–23]. Compliant compensation means taking measures to improve the surface figure accuracy of optical elements during the assembly process directly. For example, surface figure accuracy of optical elements is improved by an adjustable support mechanism or optimizing the mount structure parameters [24–26]. Reducing wavefront aberrations through either active optics or compliant compensation will increase the manufacturing costs of optical systems significantly.

During studying the surface figure compensation method of a primary mirror in a Ritchey–Chrétien space telescope, it is found that low-order aberrations of an optical surface can be improved by a simple way using spring preloads with extremely low cost, and wavefront aberrations of the optical system can be decreased significantly. Section 2 introduces a supporting structure of the primary mirror in a Ritchey–Chrétien space telescope. Section 3 presents measured surface figures of the

mirror, and analyzes the reasons for surface deformations. The epoxy in the gap between the mirror body and its central mounting hub will produce shrinkage stresses during the bonding process. Furthermore, assembly stresses generate inevitably when the central hub is installed on the mechanical structure. Both shrinkage stresses of epoxy and assembly stresses will lead to deformations of the mirror surface. To reduce the influence of the two kinds of stresses on surface figures, Section 4 puts forward a spring preload method, which introduces micro-deformation on the mirror and compensates for low-order surface figure errors by exerting appropriate pressure or tension at the specific position of the mirror. Through finite element method (FEM) analysis, the improvement effect of the preload compensation method on surface figure errors is obtained. Section 5 verifies the effectiveness of the preload compensation method and the correctness of the analysis process through experiments. Section 6 analyzes long-term stability of the mirror. Section 7 is the conclusion of this paper.

2. DESIGN AND MOUNTING OF THE PRIMARY MIRROR

This paper is based on the primary mirror of a Ritchey–Chrétien space telescope with a focal length of 1200 mm. The mirror's diameter is 190 mm. According to the design parameters and technical requirements of the Ritchey–Chrétien optical system, high alignment accuracy and high surface figure accuracy of the mirror are required in the engineering design. This Ritchey–Chrétien space telescope and its primary mirror component are shown schematically in Fig. 1.

In the mounting structure of the primary mirror, the contact surface between the mirror and its central hub is annular. In an idealized design, the gravity center of the mirror should coincide with the center of the contact surface in axial direction; if the contact surface is extended, the mirror should be divided into two parts with equal weight. In radial direction, the position of the annular surface can be calculated by Eq. (1). If the contact surface does not match Eq. (1) closely, gravity imbalance within the mirror may lead to extra surface figure errors:

$$\iiint_{\Omega_1} [S(r, \theta, z) - F(r, \theta, z)] \rho \, dr \, d\theta \, dz$$

$$= \iiint_{\Omega_2} [S(r, \theta, z) - F(r, \theta, z)] \rho \, dr \, d\theta \, dz, \quad \textbf{(1)}$$
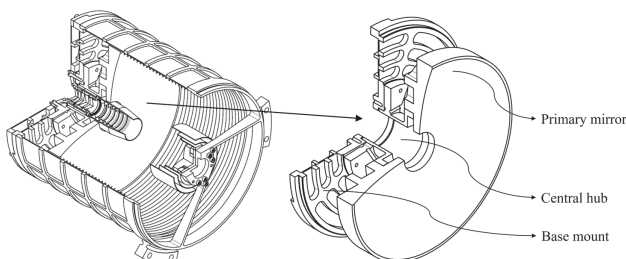

Fig. 1.   Schematic diagram of the Ritchey–Chrétien space telescope and its primary mirror component.

Table 1.   Design Parameters of the Primary Mirror

Material	Outer Diameter	Diameter of Central Hole	Vertex Radius of Curvature	Shape of Asphere
Schott Zerodur	190 mm	36 mm	−281.41 mm	Conic

where Ω_1 is an integral interval whose projection on the coordinate plane is a ring with an inner diameter of r_0 and outer diameter of r_a, Ω_2 is an integral interval whose projection on the coordinate plane is a ring with an inner diameter of r_a and outer diameter of r_1, $S(r, \theta, z)$ is the function of the optical surface in the cylindrical coordinate, $F(r, \theta, z)$ is the function of the optical surface's backside in the cylindrical coordinate, r_0 is the radius of the mirror's central hole, r_1 is the outer radius of the mirror, r_a is the radius of the contact surface between the mirror and its central hub, and ρ is the density of the mirror.

As shown in Fig. 1, the primary mirror is made of Schott Zerodur, which has a near-zero coefficient of thermal expansion (CTE); thus, the surface figure of the mirror hardly deforms with temperature variation. The central hub is made of a Super Invar alloy, which also has a near-zero CTE in a certain temperature range. The Super Invar alloy is treated with special heat processing, and its CTE is closely matched with Schott Zerodur. When temperature changes, there is very low thermal stress between the mirror and its central hub after assembly. The base mount is made of titanium alloy 6Al4V; because of its high specific stiffness, it is very helpful to design lightweight structures. Due to space and weight constraints of the space telescope, the bonding surface between the mirror and its central hub deviates from the ideal position. The design parameters of the mirror are shown in Table 1.

3. SURFACE FIGURE MEASUREMENT AND ANALYSIS

The surface shape error of the primary mirror is measured by a Zygo GPI XP interferometer and MetroPro software. The measuring principle is shown in Fig. 2, in which the secondary mirror is used as a compensator for the measurement of a conic surface. After laser rays with 632.8 nm wavelength travel through the measurement system, the reflected wavefront of the primary mirror is changed into a spherical wave, which can be measured by the interferometer. The measured result of wavefront aberrations can present surface figure errors of the primary mirror closely when the secondary mirror is of high accuracy. Measuring instruments are shown schematically in Fig. 3. The surface figure of the mirror was measured in three stages: stage I: the mirror is not bonded to its central hub; stage II: the mirror
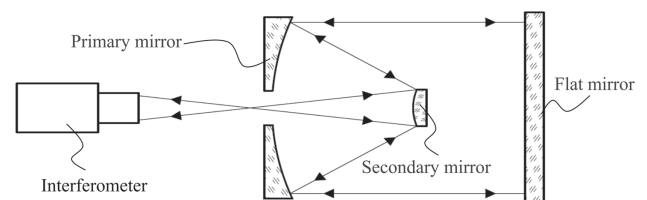

Fig. 2.   Sketch illustrating the principle of an interferometer used to measure surface figure errors of the primary mirror.
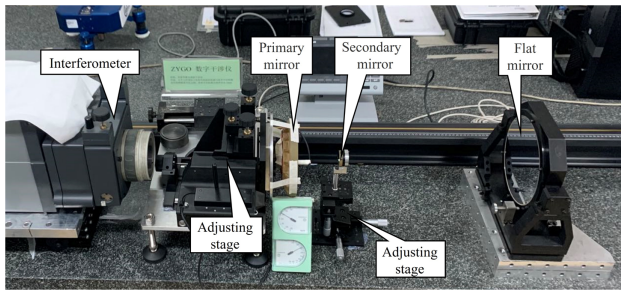
Fig. 3. Schematic diagram of measuring instruments.

is bonded to its central hub by epoxy; stage III: the central hub is assembled to the base mount after the mirror is bonded to its central hub. The measured surface figure of the primary mirror in three stages is shown in Fig. 4.

According to nodal aberration theory (NAT), there is a coma-free point in a two-mirror Ritchey–Chrétien telescope [27,28]. During alignment of the system, we adjust the tilt or the decenter of the secondary mirror until coma has been removed. Though under coma-free conditions, there may be some variations in astigmatism around the off-axis field of view, the aberration image on-axis can present the surface figure of the primary mirror closely when the secondary mirror is of high accuracy. Therefore, we regard coma as a random error during measurement and discuss the measured data without coma.

Comparing Fig. 4(a-3) with Fig. 4(b-3), we can conclude that the bonding process of the primary mirror and its central hub causes spherical aberration, high-order spherical aberrations, and a slight astigmatism. This phenomenon is mainly contributed to shrinkage stresses of the adhesive layer. If epoxy in the gap between the mirror body and its central hub has uniform thickness and shrinks uniformly, there would be spherical aberration and high-order spherical aberrations only. In reality, the thickness of epoxy is not uniform, and shrinkage stresses are not consistent due to the cylindricity error of the bonding surface, which results in a slight astigmatism.

There is a quite obvious astigmatism in the measured surface figure of stage III as shown in Fig. 4(c-3). Comparing Fig. 4(b-3) with Fig. 4(c-3), the surface figure without astigmatism or coma in stage III matches closely the surface figure without coma in stage II. It can be inferred that stresses introduced by the assembly process lead to surface deformation. The main reason for this phenomenon can be explained as follows. There are flatness errors in installation planes of the central hub and the base mount. When mounting screws are tightened, these uneven surfaces are forced to fit each other, and then local micro-deformations occur. These micro-deformations will be transferred to the mirror, resulting in astigmatism on the optical surface.

4. SPRING PRELOAD AND FEM ANALYSIS

In this part, a preload method is used to compensate for mirror deformation caused by adhesive shrinkage stresses and assembly stresses. The preloads are simulated and analyzed in UG NX, a software for finite element analysis. The coordinate values and relative displacements of the deformed surface nodes on the optical element are extracted from the simulation results.
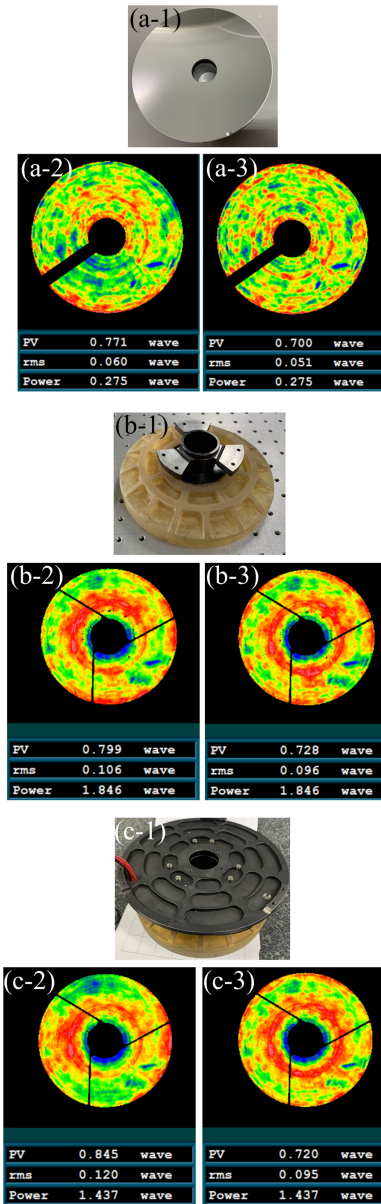

Fig. 4. Primary mirror and the measured surface figure. (a-1)–(c-1) Photos of primary mirror in stage I, stage II, and stage III; (a-2)–(c-2) measured surface figures in stage I, stage II, and stage III; (a-3), (b-3) measured surface figures without coma in stage I and stage II; (c-3) measured surface figure without astigmatism or coma in stage III.

The root mean square (RMS) values of the mirror surface are obtained by MATLAB and MetroPro software. The relation curves of the preload and RMS are fitted, and finally we get the optimized preload.

A. Finite Element Model of the Primary Mirror

Before preload analysis, we need to establish the finite element model of the primary mirror. First, we simplify the structure of the primary mirror component as shown in Fig. 1. Bolt holes, chamfered edges, and other micro-structures in the parts are simplified to mesh the parts efficiently; the bolts, which are used only to exert a clamping force, are removed, and bonding adhesive is ignored. The simplified 3D model and meshed model

for FEM are shown in Fig. 5. Fixed positions of the FEM model and the acting surface of the preload are exhibited in Fig. 5(a). Materials and main mechanical properties of the parts in the FEM model are shown in Table 2.

B. General Considerations of Gravity

To achieve an authentic measurement result of the primary mirror on the ground with the device shown in Fig. 3, the position of central hub was optimized to minimize the influence of gravity on the surface figure. Gravity-induced surface deformation of the mirror is simulated and is shown in Fig. 6. According to NAT, coma can be removed by adjusting the secondary mirror. The supporting stiffness between the primary mirror and secondary mirror has been designed to compensate for the influence of gravity on coma. The deformation result with coma removed under gravity is shown in Fig. 6(b).

From Fig. 6, it can be concluded that gravity has little influence on measurement results of the primary mirror with the device shown in Fig. 3. Actually, the influence of gravity must be removed during preload analysis, because the simulation result of gravity should not be added to the test result with gravity; otherwise, the influence of gravity will be doubled.

C. Preload Models

In this part, we define two types of preload models: ring preloads and quadrupole preloads. Ring preloads refer to forces distributed uniformly on a ring surface along the normal direction. Quadrupole preloads refer to forces distributed uniformly in the four quadrants of a ring surface along or opposite the normal direction, and the forces of the two adjacent quadrants are equal in magnitude and opposite in direction. The distributions of
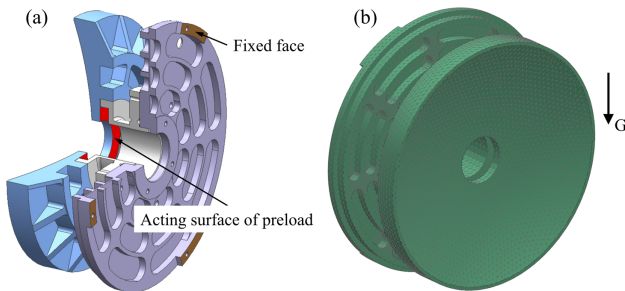

Fig. 5. Schematic diagram of FEM model: (a) fixed positions and the acting surface of preload in simplified 3D model; (b) meshed model for FEM.

Table 2.   Material Properties

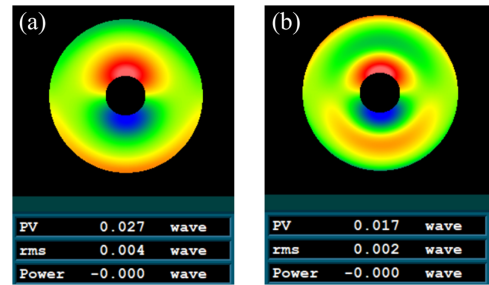| Part	Material	Density / (g·cm^{-3})	Young's Modulus E/MPa	Poisson's Ratio	CTE
Primary mirror	Schott Zerodur	2.53	90,300	0.24	0.5×10^{-7}
Central hub	Super Invar(4J32)	8.13	148,000	0.29	1.0×10^{-7}
Mount	Titanium 6A14V	4.43	114,000	0.34	8.8×10^{-6}

Fig. 6. Surface deformation of the primary mirror due to gravity: (a) gravity-induced surface deformation; (b) deformation result without coma.

preloads are shown in Fig. 7 and Table 3, where F_{Ring} represents force values of ring preloads and F_{Quad} represents force values of quadrupole preloads. We define the positive direction of preloads as the arrow directions shown in Fig. 7(a).

D. Analysis of Ring Preloads

A simulated surface figure of the primary mirror under typical ring preloads is shown in Fig. 8(a). Surface figures shown in Figs. 8(a) and 4(c-2) are expressed in terms of Zernike polynomial coefficients. As shown in Fig. 8(b), the first 36 terms of the two Zernike polynomials are compared. The surface shown in Fig. 4(c-2) is taken as the initial surface.

It can be observed from Fig. 8(b) that the ninth, 16th, 25th, and 36th terms of Zernike polynomial coefficients, which represent spherical aberration and high-order spherical aberrations, change evidently under the action of ring preloads on the primary mirror. The ninth term of Zernike polynomial coefficients of a deformed surface and initial surface have different signs ($\pm$), as well as the 16th, 25th, and 36th terms. Therefore, if we add surface figure errors of a deformed surface under the action of ring preloads to the errors of the initial surface, the surface figure errors of the initial surface would be canceled out
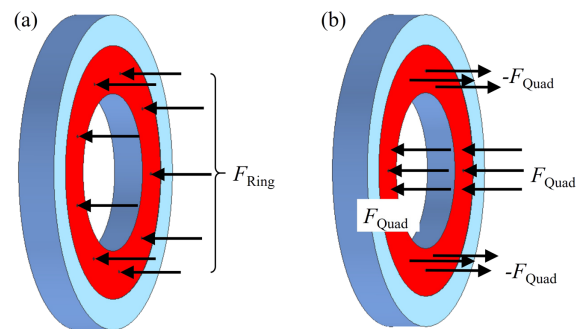

Fig. 7. Schematic diagram of preload models: (a) ring preloads; (b) quadrupole preloads.

Table 3.   Distributions of Ring Preloads and Quadrupole Preloads

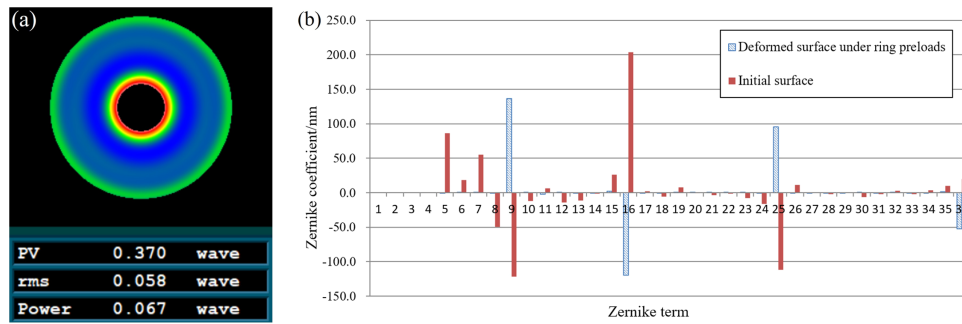|	0° ∼ 90°	90° ∼ 180°	180° ∼ 270°	270° ∼ 0°
Ring preloads		F_{Ring}		
Quadrupole preloads	F_{Quad}	$-F_{Quad}$	F_{Quad}	$-F_{Quad}$

Fig. 8. Simulation results under ring preloads: (a) surface figure of primary mirror; (b) comparison of Zernike terms of deformed surface and initial surface.
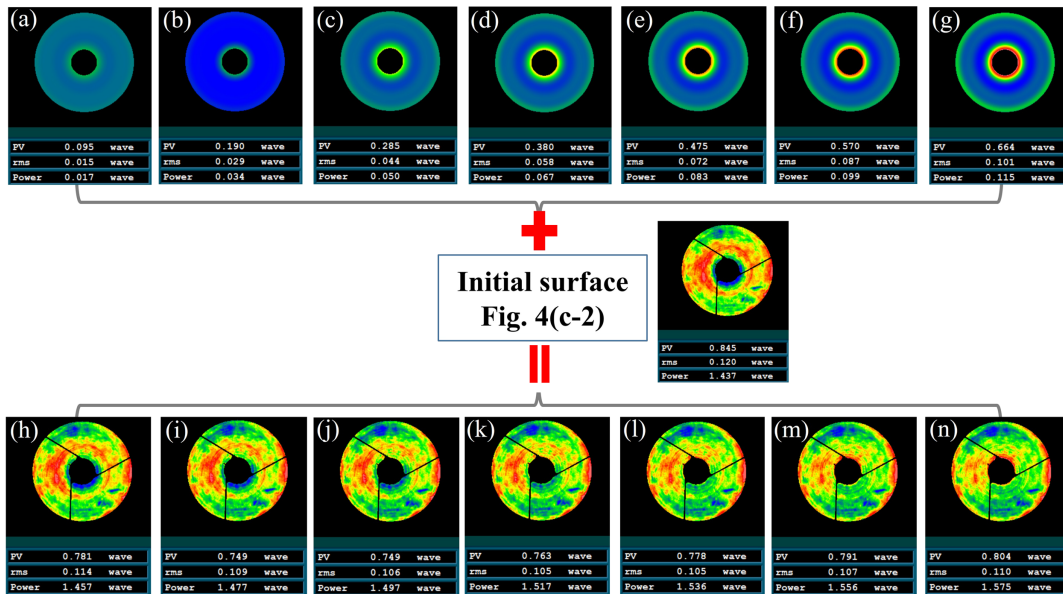

Fig. 9. Simulation and compensation results under the action of different ring preloads: (a)–(g) simulation results with F_{Ring} set to $25, 50, 75, 100,$ $125, 150, 175$ N, respectively; (h)–(n) compensation results with F_{Ring} set to $25, 50, 75, 100, 125, 150, 175$ N, respectively.

partially. So it is possible that appropriate ring preloads can partially compensate for surface figure errors caused by shrinkage stresses of the epoxy. Simulations are done by setting F_{Ring} to $25, 50, 75, 100, 125, 150,$ and 175 N. We add the surface figure errors of deformed surfaces under the action of different ring preloads to the errors of the initial surface, and get compensated surface figure errors as shown in Fig. 9.

From Fig. 9, we can conclude that ring preloads mainly compensate for spherical aberration and high-order spherical aberrations of the initial surface. The variation curve of RMS figure errors of the compensation results with F_{Ring} is shown in Fig. 10. It can be observed from Fig. 10 that with the increase of ring preloads, RMS figure errors first decrease and then increase. The compensated RMS figure error reaches to its minimum when F_{Ring} is about 108 N.

E. Analysis of Quadrupole Preloads

A simulated surface figure of the primary mirror under typical quadrupole preloads is shown in Fig. 11(a). Surface figures shown in Figs. 11(a) and 4(c-2) are expressed in terms of Zernike
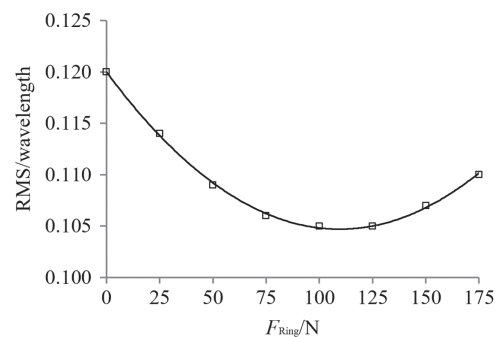

Fig. 10. Plots of RMS figure errors of the compensation results versus ring preloads.

polynomial coefficients. As shown in Fig. 11(b), the first 36 terms of the two Zernike polynomial coefficients are compared.

It can be observed from Fig. 11(b) that the fifth, sixth, 12th, 21st, and 32nd terms of Zernike polynomial coefficients change evidently under the action of quadrupole preloads on the primary mirror. The fifth term of Zernike polynomial coefficients of a deformed surface and initial surface have different signs
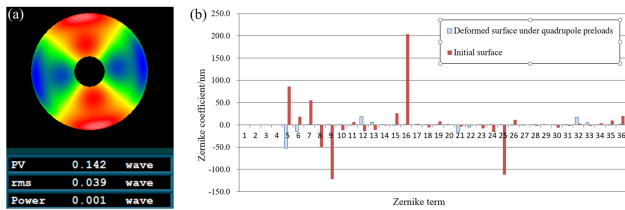
Fig. 11. Simulation results under quadrupole preloads: (a) surface figure of primary mirror; (b) comparison of Zernike terms of deformed surface and initial surface.

($\pm$), as well as the sixth. The fifth and sixth terms of Zernike polynomial coefficients represent astigmatism. Therefore, if we add surface figure errors of a deformed surface under the action of quadrupole preloads to the errors of the initial surface, the surface figure errors of the initial surface would be canceled out partially. So it is possible that appropriate quadrupole preloads can partially compensate for surface figure errors caused by the assembly process.

According to the astigmatism direction of the initial surface, the quadrupole preload distribution is rotated by 6° around the mirror center, so that the angle between the astigmatism direction of a deformed surface and initial surface is about 90°. Simulations are done by setting F_{Quad} to 3, 6, 9, 12, 15, 18, and 21 N. We add the surface figure errors of deformed surfaces under the action of different quadrupole preloads to the errors of the initial surface, and get compensated surface figure errors as shown in Fig. 12.

From Fig. 12, we can conclude that quadrupole preloads mainly compensate for astigmatism of the initial surface. The variation curve of RMS figure errors of the compensation results with F_{Quad} is shown in Fig. 13. It can be observed from Fig. 13 that with the increase of quadrupole preloads, RMS figure errors first decrease and then increase. The compensated RMS figure error reaches its minimum when F_{Quad} is about 10.5 N.

F. Analysis of Combined Preloads

According to the optimized preloads determined in Figs. 9 and 11, we combine the optimized quadrupole preloads with the optimized ring preloads, and the combined results are shown in Table 4, where quadrupole preloads are rotated by 6° to match the astigmatism direction of the initial surface.

The simulated surface figure of the primary mirror under combined preloads is shown in Fig. 14(a). We add the surface figure errors of a deformed surface under the action of combined preloads to the errors of the initial surface, and get compensated surface figure errors as shown in Fig. 14(b).

To further study the effect of combined preloads, the first 36 terms of Zernike polynomial coefficients of a deformed surface under combined preloads, initial surface, and compensated surface of simulation are shown in Fig. 15. It can be observed from Fig. 15 that under the action of combined preloads, the fifth term (0°astigmatism), sixth term (45 °astigmatism), ninth term (spherical aberration), 16th term (higher-order spherical aberration), 25th term (higher-order spherical aberration), and 36th term (higher-order spherical aberration) of Zernike polynomial coefficients of the initial surface decrease obviously in absolute value. The figure error of the initial surface is improved from RMS to 0.088λ RMS at λ = 632.8 nm under the action of combined preloads.

G. Influences of Temperature Variations

Figure 14(a) is the simulation result at 20°C. When the temperature variations are ±5?, surface deformations of the primary mirror are analyzed without preloads and with combined preloads, respectively. The simulation results are shown in Fig. 16.

From Fig. 16, two conclusions can be drawn as follows: (1) when the temperature variations are ±5°C, the surface figure error changes about 0.088λ RMS, which is relatively small, and
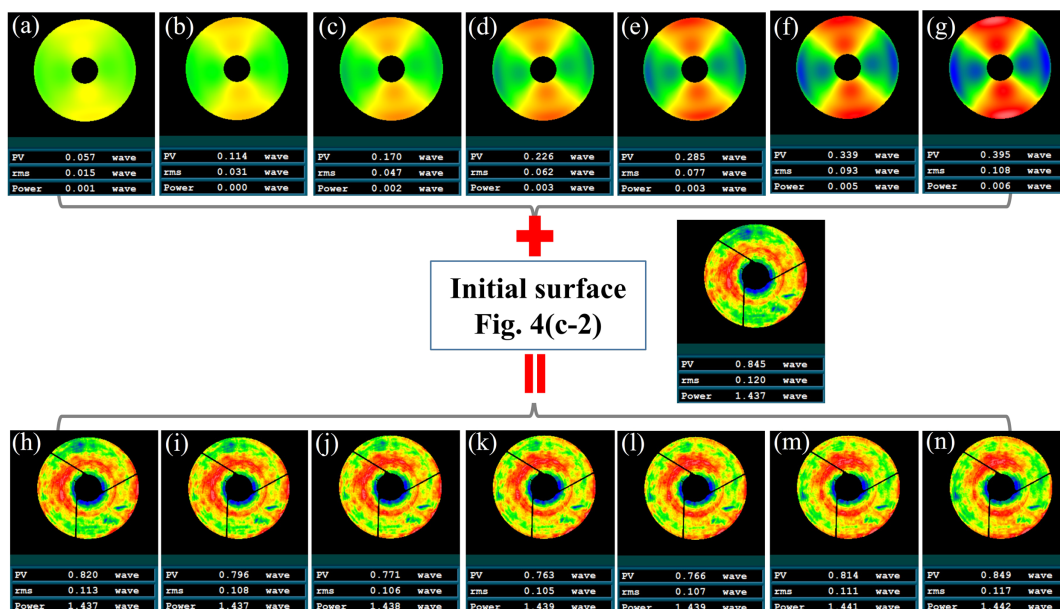

Fig. 12. Simulation and compensation results under the action of different quadrupole preloads: (a)–(g) simulation results with F_{Quad} set to 3, 6, 9, 12, 15, 18, 21 N, respectively; (h)–(n) compensation results with F_{Quad} set to 3, 6, 9, 12, 15, 18, 21 N, respectively.
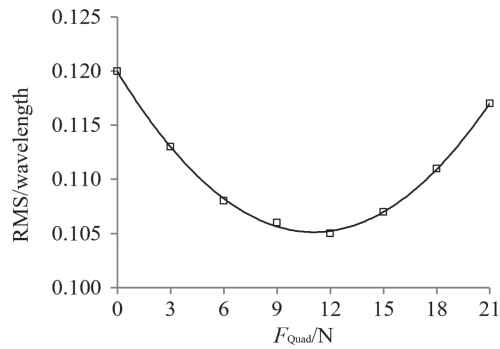
Fig. 13. Plots of RMS figure errors of the compensation results versus quadrupole preloads.

Table 4. Optimized Preloads and their Combinations

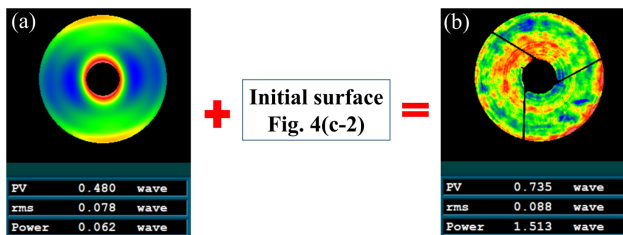|	6°–96°	96°–186°	186°–276°	276°–366°
Ring preloads		108 N		
Quadrupole preloads	10.5 N	−10.5 N	10.5 N	−10.5 N
Combined preloads	37.5 N	16.5 N	37.5 N	16.5 N

Fig. 14. Simulation and compensation results under the action of combined preloads: (a) simulation result; and (b) compensation result by simulation.
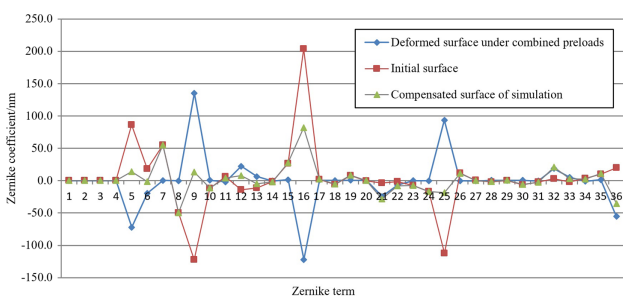

Fig. 15. Zernike coefficients of different surface figures.

the camera can perform properly with thermal control measures on the satellite; (2) influences of temperature variations and preloads are mutually independent. The compensation method in this paper is still effective within a certain temperature variation.

5. EXPERIMENT OF COMBINED PRELOADS

In this part, we design and conduct an experiment to verify the compensation effect of the primary mirror under the action of
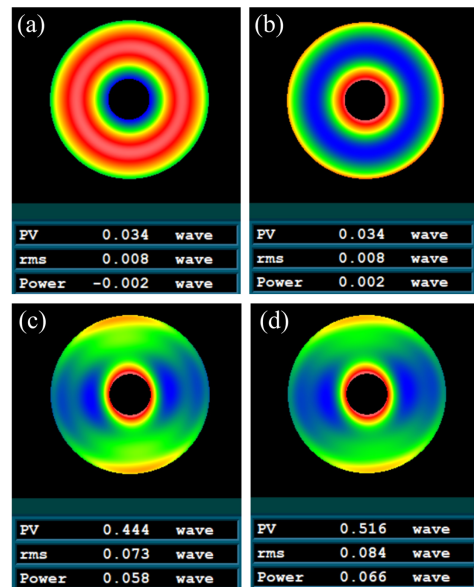

Fig. 16. Surface deformation of the primary mirror due to temperature variation: (a), (b) simulation results of the ideal surface at 25°C and 15°C, respectively; (c), (d) simulation results under the action of combined preloads at +5°C and −5°C, respectively.

combined preloads shown in Table 4. To exert the combined preloads, we put 12 different compression springs between the acting surface of the preload and the central hub. The springs are distributed uniformly around the mirror center and bonded to the central hub with epoxy; there are also other mechanical structures on the space telescope to maintain the positions of the springs under the vibration of transportation and launch. Distribution angles and preloads of the 12 springs are shown in Table 5. A schematic diagram of the installation is shown in Fig. 17.

After installing preload springs on the primary mirror, surface figure errors are measured by an interferometer. The compensation result of the experiment is shown in Fig. 18(a). The first 36 terms of Zernike polynomial coefficients of compensated surfaces of the experiment, initial surface, and compensated surface of simulation are shown in Fig. 18(b).

Comparing Figs. 18(a) and 4(c-2), it can be observed that the figure error of the initial surface is improved from 0.120λ RMS to 0.084λ RMS at $\lambda = 632.8$ nm under spring preloads. The compensation result of the experiment is close to the result of simulation shown in Fig. 14(b). It can be observed from Fig. 18(b) that the preload compensation method presented in this paper can compensate for part of the astigmatism, spherical aberration, and high-order spherical aberrations simultaneously. There is a minor difference between compensation results of the experiment and simulation, which can be attributed to the following: (1) the properties of epoxy are not considered in the simulation model, but in fact, the adhesive affects the stresses and strains transferred to the mirror; (2) the preloads are consecutive in the simulation, but they are realized discretely by 12 springs in the experiment, and there are also errors in the magnitudes and installation positions of the springs; (3) the tilt or the decenter of the secondary mirror will lead to random

Table 5.   Distribution Angles and Preloads of the 12 Springs

Spring No.	1	2	3	4	5	6	7	8	9	10	11	12
Angle	21°	51°	81°	111°	141°	171°	201°	231°	261°	291°	321°	351°
Preload/N	12.5	12.5	12.5	5.5	5.5	5.5	12.5	12.5	12.5	5.5	5.5	5.5
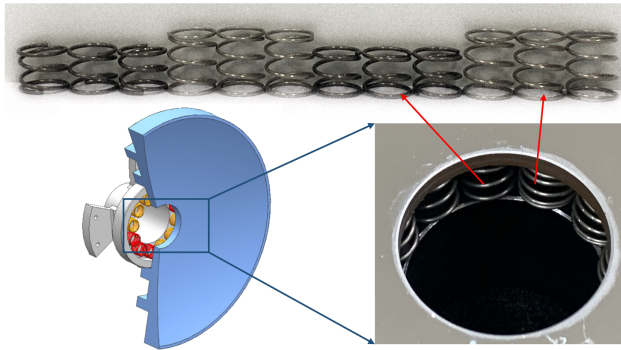
Fig. 17.   Schematic diagram of the installation of the 12 springs.
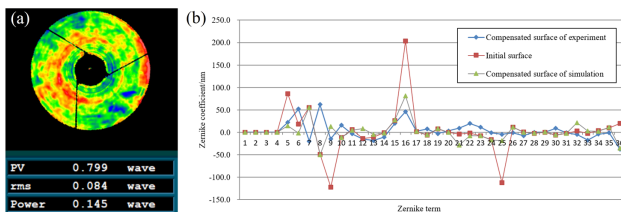
Fig. 18.   Experiment result: (a) compensation result of experiment; and (b) Zernike coefficients of different surface figures.

coma during each alignment process. In summary, the experimental result shows that the preload method presented in this paper can effectively compensate for part of the surface figure error caused by the assembly process and significantly improve the surface figure accuracy of the primary mirror.

6. CONSIDERATIONS OF LONG-TERM STABILITY

As the mirror is utilized under applied stresses, the creep behavior of glass must be considered during long-term usage. Theoretically, it is usually assumed that the creep rate is a function of three independent variables, i.e., temperature, stress, and material constant. The creep rate is represented as the following expression [29]:

$$\dot{\varepsilon}_c = A\sigma^n \exp[-Q_c/(RT)], \qquad (2)$$

where $\dot{\varepsilon}_c$ is the creep rate, A is a constant for a given material, σ is the applied stress, n is the stress exponent, Qc is the activation energy, T is the material temperature, and R is Boltzmann's constant.

According to the simulation result, the maximum stress in the mirror is 0.59 Mpa under the action of combined preloads, and T is about 20°C. Therefore, the creep rate is rather small according to Eq. (2), and the mirror will not have obvious creep within service life of the satellite. After applying the combined preloads for 3 months, the surface figure of the mirror was measured and
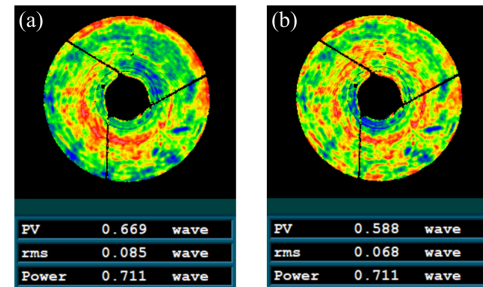
Fig. 19.   Experiment result after applying the combined preloads for 3 months: (a) surface figure error with coma; (b) surface figure error without coma.

the result is shown in Fig. 19. Except for the orientation of coma, which can be regarded as a random error, there are barely any changes in surface figure errors. It can be concluded that the mirror can maintain high stability and reliability in long-term usage under the action of combined preloads.

7. CONCLUSION

In conclusion, we propose a preload compensation method to improve the surface figure accuracy of the primary mirror with a radius of 190 mm in a Ritchey–Chrétien space telescope. The surface figure of the primary mirror deteriorates evidently during the assembly process due to adhesive shrinkage stresses and assembly stresses. Simulation results of the preload compensation method indicate that ring preloads mainly affect spherical aberration and high-order spherical aberrations, and quadrupole preloads mainly affect astigmatism. The combination of optimal ring preloads, and quadrupole preloads can compensate for figure errors of the primary mirror properly. The correctness of the analysis process and the effectiveness of the compensation method are verified by an experiment, which improves the figure error from 0.120λ RMS to 0.084λ RMS at $\lambda = 632.8$ nm under the action of 12 springs.

REFERENCES

1. W.-C. Lin, S.-T. Chang, S.-H. Chang, C.-P. Chang, Y.-C. Lin, C.-C. Chin, H.-P. Pan, and T.-M. Huang, "Alignment and assembly process for primary mirror subsystem of a spaceborne telescope," Opt. Eng. **54**, 115109 (2015).
2. H. Choi, I. Trumper, Y.-T. Feng, H. Kang, J. Berkson, H. Chung, E. Hamden, and D. Kim, "Long-slit cross-dispersion spectroscopy for Hyperion UV space telescope," J. Astron. Telesc. Instrum. Syst. **7**, 014006 (2021).

3. S. Jeong, J. W. Nam, K. B. Ahn, *et al.*, "Slewing mirror telescope optics for the early observation of UV/optical photons from gamma-ray bursts," Opt. Express **21**, 2263–2278 (2013).

4. F. Pirondini, J. López, E. González, and J. Antonio González, "DEIMOS-2: cost-effective, very-high resolution multispectral imagery," Proc. SPIE **9241**, 92411C (2014).

5. M. Shao, L. Zhang, and X. Jia, "Opto-mechanical integrated optimization of a lightweight mirror for space camera," Appl. Opt. **60**, 539–546 (2020).

6. Chang, K. Bruna, X. Zhong, F. Li, W. Sun, and H. de Beaufort, "Future EO system: the first VHR CCD camera constellation of 138 microsatellite," *72nd International Astronautical Congress (IAC)*, Dubai, UAE, October 25–29, 2021.

7. G. Tyc, J. Tulip, D. Schulten, M. Krischke, and M. Oxfort, "The RapidEye mission design," Acta Astronaut. **56**, 213–219 (2005).

8. Y. Xue, Y. Li, J. Guang, X. Zhang, and J. Guo, "Small satellite remote sensing and applications—history, current and future," Int. J. Remote Sens. **29**, 4339–4372 (2008).

9. S. Gensemer and M. Gross, "Figuring large optics at the sub-nanometer level: compensation for coating and gravity distortions," Opt. Express **23**, 31171–31180 (2015).

10. G. Qiao, H. Hu, X. Zhang, X. Luo, D. Xue, G. Zhang, H. Hu, L. Yi, Y. Yang, and W. Deng, "Stress-induced deformation of coating on large lightweight freeform optics," Opt. Express **29**, 4755–4769 (2021).

11. C. Reinlein, C. Damm, N. Lange, A. Kamm, M. Mohaupt, A. Brady, M. Goy, N. Leonhard, R. Eberhardt, U. Zeitner, and A. Tünnermann, "Temporally-stable active precision mount for large optics," Opt. Express **24**, 13527–13541 (2016).

12. K.-W. Chan, W. W. Zhang, T. T. Saha, R. S. McClelland, M. P. Biskach, J. Niemeyer, M. J. Schofield, J. R. Mazzarella, L. D. Kolos, M. M. Hong, A. Numata, M. V. Sharpe, P. M. Solly, R. E. Riveros, K. D. Allgood, and K. P. McKeon, "Aligning, bonding, and testing mirrors for lightweight x-ray telescopes," Proc. SPIE **9603**, 96030Z (2015).

13. Z. Fan, Y. Dai, C. Guan, G. Tie, and J. Liu, "Effect of the adhesive layer on the unimorph deformable mirror," Optik **160**, 77–85 (2018).

14. S. Tan, X. Yu, Y. Xu, Y. Xu, and P. Jia, "Micro-stress bonding analysis of high precision and lightweight mirrors," Opt. Express **29**, 33665–33678 (2021).

15. L.-J. Feng, J.-T. Ding, and G.-Y. Zou, "Design of SiC mirror subsystem of a space-based astronomy telescope," Proc. SPIE **10837**, 108370A (2019).

16. J. H. Clark, III, F. Ernesto Penado, M. DiVitorrio, and J. P. Walton, "Mount-induced deflections in 8-inch flat mirrors at the navy prototype optical interferometer," Proc. SPIE **7013**, 70133K (2008).

17. X. Hu, Z. Wu, L. Chen, and B. Zhang, "A self-correction method for deformable mirror with thermal deformation," Optik **145**, 632–643 (2017).

18. J. Schwarz, M. Geissel, P. Rambo, and J. Porter, "Development of a variable focal length concave mirror for on-shot thermal lens correction in rod amplifiers," Opt. Express **14**, 10957–10969 (2006).

19. J. H. Clark, III and F. Ernesto Penado, "Compliant deformable mirror approach for wavefront improvement," Opt. Eng. **55**, 043107 (2016).

20. J. Schwarz, M. Ramsey, I. Smith, D. Headley, and J. Porter, "Low order adaptive optics on Z-Beamlet using a single actuator deformable mirror," Opt. Commun. **264**, 203–212 (2006).

21. D. R. Neill, G. Muller, E. Hileman, J. DeVries, C. Araujo, W. J. Gressler, P. J. Lotz, D. Mills, J. Sebag, S. Thomas, M. Warner, and O. Wiecha, "Final design of the LSST primary/tertiary mirror cell assembly," Proc. SPIE **9906**, 99060Q (2016).

22. K. Ahn and H. Kihm, "Moment actuator for correcting low-order aberrations of deformable mirrors," Opt. Lasers Eng. **126**, 105864 (2020).

23. M. Laslandes, K. Patterson, and S. Pellegrino, "Optimized actuators for ultrathin deformable primary mirrors," Appl. Opt. **54**, 4937–4952 (2015).

24. H. Kihm, H.-S. Yang, I. K. Moon, J.-H. Yeon, S.-H. Lee, and Y.-W. Lee, "Adjustable bipod flexures for mounting mirrors in a space telescope," Appl. Opt. **51**, 7776–7783 (2012).

25. Z. Feng, Y. Jie, W. Li-Ping, L. Yuan-Ming, Z. Hai-Tao, M. Quan, L. Qiang, B. Ran, W. Hui, and J. Chun-Shui, "Adjustable flexure mount to compensate for deformation of an optic surface," Appl. Opt. **58**, 9370–9375 (2019).

26. J. H. Burge, B. Cuerden, and J. R. P. Angel, "Active mirror technology for large space telescopes," Proc. SPIE **4013**, 640–648 (2000).

27. T. Schmid, K. P. Thompson, and J. P. Rolland, "A unique astigmatic nodal property in misaligned Ritchey-Chrétien telescopes with misalignment coma removed," Opt. Express **18**, 5282–5288 (2010).

28. N. Zhao, J. C. Papa, K. Fuerschbach, Y. Qiao, K. P. Thompson, and J. P. Rolland, "Experimental investigation in nodal aberration theory (NAT) with a customized Ritchey-Chrétien system: third-order coma," Opt. Express **26**, 8729–8743 (2018).

29. T. Rouxel, M. Huger, and J. L. Besson, "Rheological properties of Y-Si-Al-O-N glasses-elastic moduli, viscosity and creep," J. Mater. Sci. **27**, 279–284 (1992).